Comparison of finite difference and finite element methods for simulating two-dimensional scattering of elastic waves

Marcel Frehner [a,*], Stefan M. Schmalholz [a], Erik H. Saenger [a,b], Holger Steeb [c]

[a] *Geological Institute, Department of Earth Sciences, ETH Zurich, 8092 Zurich, Switzerland*
[b] *Spectraseis AG, 8005 Zurich, Switzerland*
[c] *Multi Scale Mechanics, TS, CTW, University of Twente, 7500 AE Enschede, The Netherlands*

A R T I C L E   I N F O

A B S T R A C T

Two-dimensional scattering of elastic waves in a medium containing a circular heterogeneity is investigated with an analytical solution and numerical wave propagation simulations. Different combinations of finite difference methods (FDM) and finite element methods (FEM) are used to numerically solve the elastodynamic wave equations. Finite difference and finite element techniques are applied to approximate both the time and space derivatives and are combined in various ways to provide different numerical algorithms for modeling elastic wave propagation. The results of the different numerical algorithms are compared for simulations of an incident plane P-wave that is scattered by a mechanically weak circular inclusion whereby the diameter of the inclusion is of the same order than the P-wave's wavelength. For this scattering problem an analytical solution is available and used as the reference solution in the comparison of the different numerical algorithms. Staircase-like spatial discretization of the inclusion's circular shape with the finite difference method using a rectangular grid provides accurate velocity and displacement fields close to the inclusion boundary only for very high spatial resolutions. Implicit time integration based on either finite differences or finite elements does not provide computational advantages compared to explicit schemes. The best numerical algorithm in terms of accuracy and computation time for the investigated scattering problem consists of a finite element method in space using an unstructured mesh combined with an explicit finite difference method in time. The computational advantages and disadvantages of the different numerical algorithms are discussed.

© 2008 Elsevier B.V. All rights reserved.

1. Introduction

Propagation of seismic waves can be described analytically for some specific geometrical setups (Love, 1927; Achenbach, 1973; Aki and Richards, 1980; Ben-Menahem and Jit Singh, 1981). For more complex geometries, ray-tracing methods (Moser and Pajchel, 1997; Cerveny, 2001) are able to approximate propagation of high-frequency seismic waves when the wavelength is significantly smaller than the characteristic size of heterogeneities. For seismic waves having a significantly larger wavelength than the characteristic size of heterogeneities, effective medium theories can be used (Mavko et al., 1998). However, if the wavelengths of the propagating waves and the characteristic size of heterogeneities are of the same order, numerical methods are essential. Particular numerical challenges are for example scattering phenomena in complex geometries (Korneev and Johnson, 1996), wave attenuation due to

wave induced fluid flow (Carcione et al., 2003; Masson and Pride, 2007), wave propagation in three-phase media (Carcione et al., 2004; Santos et al., 2005) or microscale modeling of wave propagation in poroelastic rocks (Saenger et al., 2007). Although on different scales, all these challenges comprise wave scattering at heterogeneities.

For numerical modeling of seismic wave propagation different methods are available (Kelly and Marfurt, 1990; Carcione et al., 2002; Cohen, 2002) which can have advantages and disadvantages depending on the particular problem under study. Methods used in this paper are the finite difference method (FDM) (Smith, 1985; Ames, 1992; Moczo et al., 2007) and the finite element method (FEM) (Hughes, 1987; Bathe, 1996; Zienkiewicz and Taylor, 2000). Both methods can be used to discretize spatial as well as time derivatives. Different combinations of spatial and temporal discretization methods using FDM and FEM are compared in this study. The different algorithms are described and applied to a two-dimensional (2D) elastic scattering problem for comparison. Analytical solutions for scattered wave fields are available for different cases (Ying and Truell, 1956; White, 1958; Liu et al., 2000;

---

* Corresponding author. Tel.: +41 44 632 88 72; fax: +41 44 632 10 30.
E-mail address: marcel.frehner@erdw.ethz.ch (M. Frehner).

Sanchez-Sesma and Iturraran-Viveros, 2001). Liu et al. (2000) provide an analytical solution to the particular 2D scattering problem considered in this study. It is used as the reference solution for the comparison of the numerical results.

The main aim of this study is to compare results of numerical wave propagation simulations based on different numerical algorithms and to discuss accuracy and computational performance of the different algorithms for a particular scattering problem. The investigated 2D scattering problem consists of a mechanically weak circular inclusion embedded in a stiffer elastic medium whereby a plane P-wave is scattered by the inclusion having a diameter similar to the P-wave's wavelength.

2. Model setup

Fig. 1a displays a snapshot of a numerical wave propagation simulation showing the 2D model used in this study. The model consists of a mechanically weak circular inclusion with radius $a = 25$ m embedded in a homogeneous elastic medium. A synthetic receiver placed outside the inclusion records the particle displacement in both x- and y-directions. Boundary conditions are free surface at $y = L_y$ (all stresses $\sigma = 0$), rigid boundary at $y = 0$ (all displacements $u = 0$) and free slip at $x = 0$ and $x = L_x$ (displacement in x-direction $u_x = 0$ and shear stress $\sigma_{xy} = 0$). All physical parameters are given in Table 1. The surrounding material represents an average sedimentary rock with the two Lamé constants λ_1 and μ_1 equal to each other. The inclusion represents a hole filled with gas that is approximated with a shear modulus $\mu_2 = 0$ and Lamé constant λ_2 1000 times smaller compared to the surrounding rock.

Instead of applying an external force (i.e. force term in the elastodynamic wave equation) an initial perturbation in the particle velocity field in y-direction is prescribed at $y = L_y$. The resulting plane P-wave is a Ricker wavelet with a dominant wavelength of $\lambda_{dom} = 157.1$ m (dominant frequency $f_{dom} = 26.8$ Hz). Fig. 1b shows a snapshot of the resulting plane P-wave travelling from the bottom of the model towards the top, and being scattered at the inclu-

sion. Clearly visible is the direct plane P-wave that stays relatively undisturbed behind the heterogeneity, and the primary scattered P-wave and S-wave (P-to-S-converted) that are emitted in all directions from the circular inclusion. In addition, a part of the wave is trapped inside the inclusion.

3. Methods

All numerical methods applied here discretize the linear elastodynamic wave equations in 2D (Love, 1927; Lindsay, 1960; Achenbach, 1973) given by

$$
\begin{Bmatrix} \rho \dfrac{\partial^2 u_x}{\partial t^2} \\ \rho \dfrac{\partial^2 u_y}{\partial t^2} \end{Bmatrix}
$$

$$
= \begin{Bmatrix} \dfrac{\partial}{\partial x}\left((\lambda + 2\mu)\dfrac{\partial u_x}{\partial x} + \lambda \dfrac{\partial u_y}{\partial y} \right) + \dfrac{\partial}{\partial y}\left(\mu\left(\dfrac{\partial u_x}{\partial y} + \dfrac{\partial u_y}{\partial x}\right) \right) \\ \dfrac{\partial}{\partial y}\left(\lambda \dfrac{\partial u_x}{\partial x} + (\lambda + 2\mu)\dfrac{\partial u_y}{\partial y} \right) + \dfrac{\partial}{\partial x}\left(\mu\left(\dfrac{\partial u_x}{\partial y} + \dfrac{\partial u_y}{\partial x}\right) \right) \end{Bmatrix}.
\tag{1}
$$

Variable ρ is density, t is time, x and y are the spatial coordinates and λ and μ are the two Lamé constants, where μ is commonly referred to as the shear modulus. The applied numerical algorithms are based on the FDM and the FEM but use different combinations of the two methods for discretizing space and time derivatives. Three basically different algorithms are applied:

(1) Explicit FDM in time, FDM in space.
(2) Explicit or implicit FDM in time, FEM in space.
(3) FEM in time, FEM in space.

3.1. Explicit FDM in time and FDM in space

For the FDM in space Eq. (1) is split into five first-order differential equations using the velocity–stress formulation. The numerical
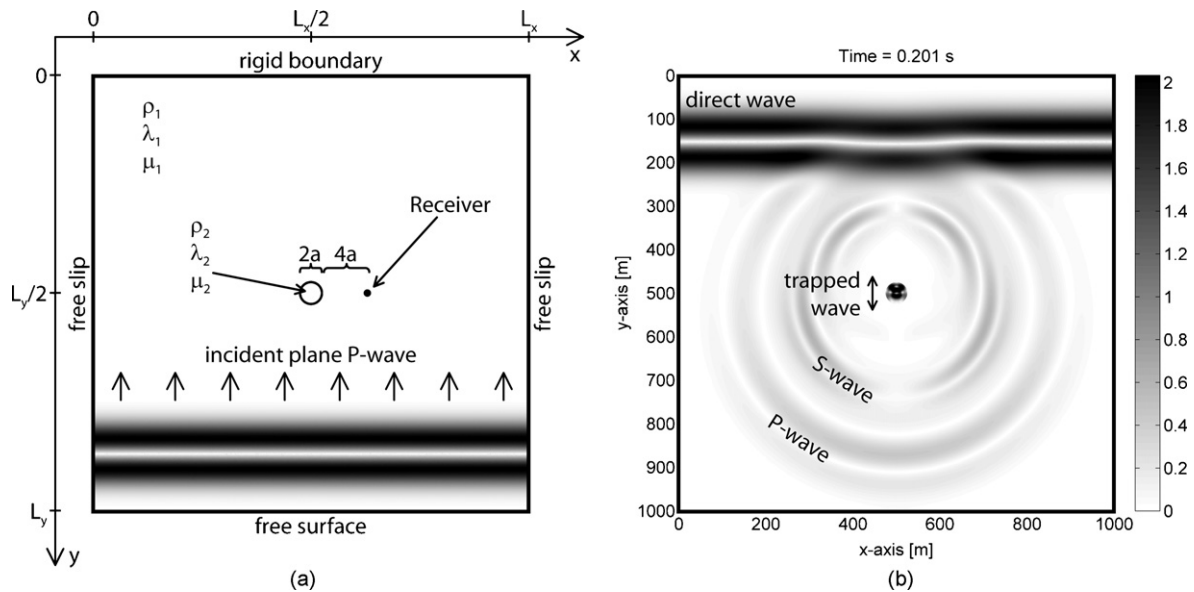

Fig. 1. Two representative snapshots of the wave field to illustrate the numerical setup. The particular method used to generate this figure is the spatial FEM with the implicit FDM in time. Plotted is the normalized absolute value of the displacement field ($10^{12}\sqrt{u_x^2 + u_y^2}$). (a) Early snapshot of the simulation to show the model setup used for all simulations. A plane P-wave travels from bottom to top of the model. Values for indicated physical parameters are given in Table 1. Black dot to the right of the inclusion is a synthetic receiver used for further analysis and has a distance to the center of the inclusion of five times the radius a. (b) Snapshot after 0.201 s to show the wave field under study. Values higher than 2 (maximal amplitude of incident wave) are reduced to 2 and colored in black. Amplitudes inside circular inclusion are higher than the gray scale indicates.

Table 1
Geometrical and physical properties used for the scattering modeling

Parameter	Value
Model size in x-direction	$L_x = 1000\,\text{m}$
Model size in y-direction	$L_y = 1000\,\text{m}$
Radius of inclusion	$a = 25\,\text{m}$
Density of surrounding media	$\rho_1 = 2700\,\text{kg/m}^3$
Density of inclusion	$\rho_2 = \rho_1/100$
Lamé constant λ of surrounding media	$\lambda_1 = 16\,\text{GPa}$
Lamé constant λ of inclusion	$\lambda_2 = \lambda_1/1000$
Lamé constant μ of surrounding media (=shear modulus)	$\mu_1 = 16\,\text{GPa}$
Lamé constant μ of inclusion (=shear modulus)	$\mu_2 = 0\,\text{Pa}$
P-wave velocity of surrounding medium	$V_{P1} = 4216\,\text{m/s}$
P-wave velocity of inclusion	$V_{P2} = 770\,\text{m/s}$
S-wave velocity of surrounding medium	$V_{S1} = 2434\,\text{m/s}$
S-wave velocity of inclusion	$V_{S2} = 0\,\text{m/s}$

method commonly used to model wave propagation is the FDM on a staggered grid (Virieux, 1986) using the explicit FDM for time discretization. For this method the two components of the 2D velocity field are defined at different discrete positions within the grid. Components of the stress tensor are also defined at different positions. This implies that both density and shear modulus have to be defined at more than one position in an elementary cell (Virieux, 1986). For modeling high material contrasts special averaging methods of these parameters (Moczo et al., 2002) are necessary to avoid numerical stability problems. Saenger et al. (2000) proposed a modified staggered grid method, i.e. the rotated staggered grid (RSG), for which all components of one physical property are defined at the same position in the grid. No averaging of elastic moduli is necessary. Bohlen and Saenger (2006) presented a stability and accuracy study and demonstrated that the RSG method is more accurate compared to the standard staggered grid method.

The FDM used in this paper is equivalent to the RSG-FDM. Fig. 2 shows the elementary cell of the grid. Crosses indicate positions where spatial derivatives of the five unknowns (v_x, v_y, σ_{xx}, σ_{yy} and σ_{xy}) are calculated. The spatial derivatives are averaged to nodal points (for spatial derivatives of stress components) or to center points (for spatial derivatives of velocity components), respectively, to multiply them with the appropriate material parameter.
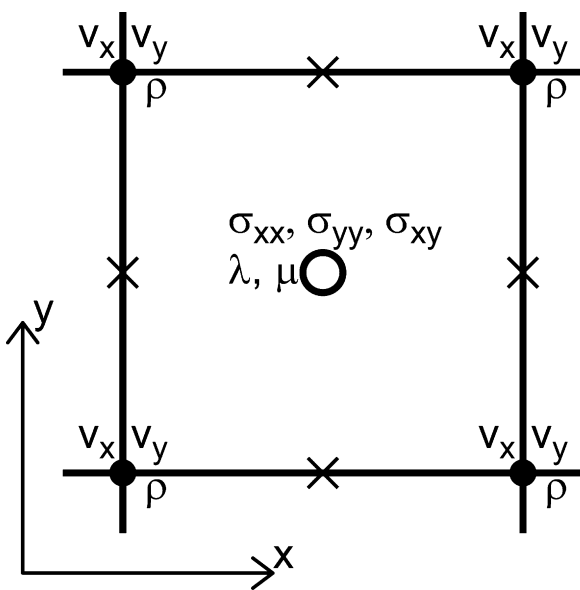

Fig. 2. Elementary cell for the applied staggered grid FDM. All components of one physical property are defined at the same position in the elementary cell. Spatial derivatives of all unknowns are defined at positions marked with a cross and have to be arithmetically averaged to nodal or center points.
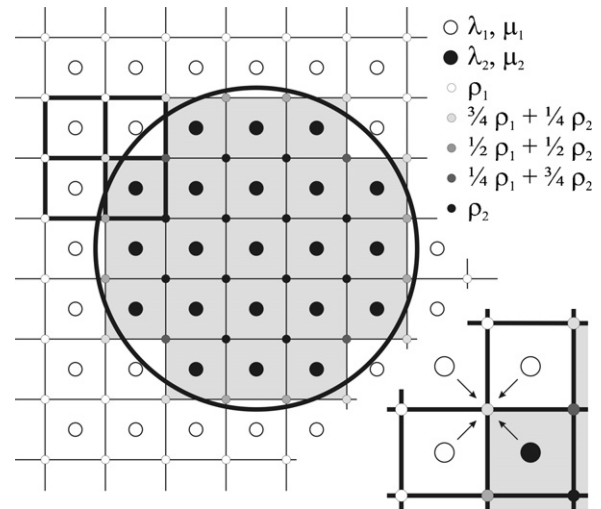

Fig. 3. Sketch of discretization of material properties with the applied staggered grid FDM. Big black circle is the inclusion with different material properties than the surrounding medium. Shaded area represents the numerical discretization of the same inclusion. Discretization runs along boundaries between elementary cells. Elastic moduli are defined on big dots (center points) and density is defined on small dots (nodal points). Four elementary cells are blown up to illustrate the arithmetic averaging of the density.

Fig. 3 sketches the discretization of properties in an inhomogeneous medium. Each elementary cell belongs to one of the two media. In other words, the boundary between different media is discretized along boundaries between elementary cells. According to Kruger et al. (2005), elastic moduli are defined at the center of each elementary cell and can only have the value of either of the two media. Therefore, no averaging of elastic moduli is necessary. Density is defined at nodal points of the grid and has to be arithmetically averaged at nodal points where the four surrounding elementary cells do not belong to the same medium (Kruger et al., 2005). This spatial discretization method is not restricted to equally spaced grids but allows changes in spatial resolution, e.g. higher resolution towards the inclusion. However, the grid is always rectangular, which leads to a staircase-like discretization of the circular inclusion. First-order time derivatives are discretized using the explicit FDM together with a staggered method in time. The von Neumann stability criterion (Higham, 1996; Saenger et al., 2000) is used to define the maximum time increment for stable solutions.

3.2. Implicit and explicit FDM in time and FEM in space

The FEM for spatial discretization used in this study (Hughes, 1987; Bathe, 1996; Zienkiewicz and Taylor, 2000) employs 7-node isoparametric triangular elements with biquadratic continuous interpolation functions (Zienkiewicz and Taylor, 2000). Numerical grids are generated by the software Triangle (Shewchuk, 1996, 2002) that produces Delaunay-type meshes. Fig. 4 sketches the spatial discretization of the circular inclusion with an unstructured triangular grid. Such grids allow strong spatial resolution changes over relatively short distances, e.g. higher resolution close to the inclusion boundary. Numerical implementation comprises the Galerkin weighted residual method (Zienkiewicz and Taylor, 2000), lumped mass matrix (Bathe, 1996; Cohen, 2002) and Gauss–Legendre quadrature with seven integration points (Zienkiewicz and Taylor, 2000). Compared to the FDM described above, material properties are defined for each element and not on individual nodal points. Therefore, no interpolation and averaging of these properties is necessary because the numerical mesh is
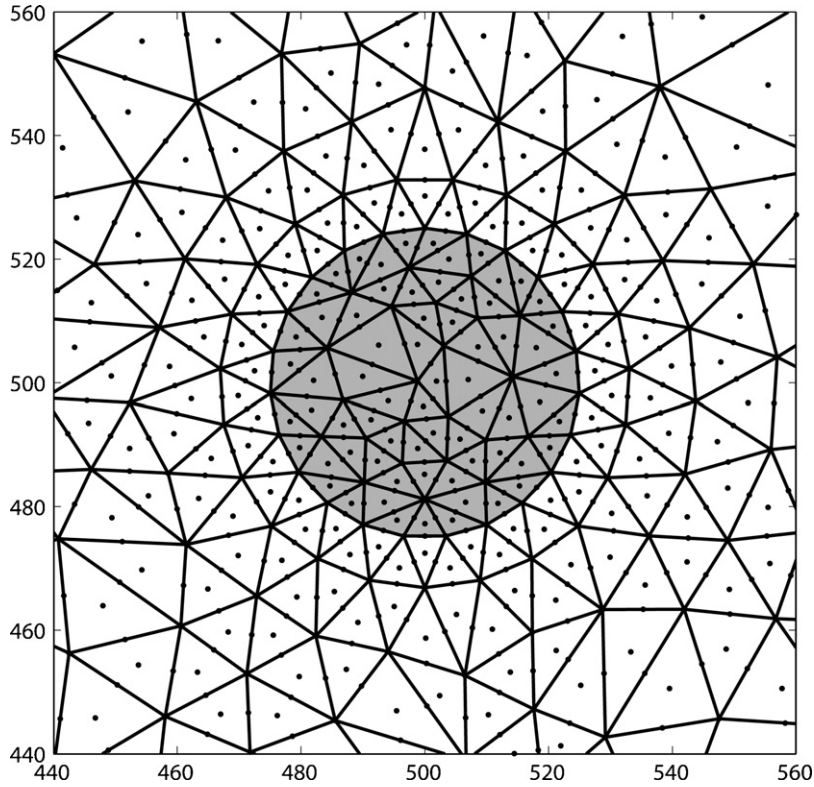
Fig. 4. Sketch of discretization of inhomogeneity using an unstructured triangular FEM-mesh. Each triangle consists of seven nodal points on which the displacement is calculated. Spatial resolution can increase towards the inclusion boundary that leads to a very accurate discretization of the boundary without the need of a high resolution away from the boundary.

generated in such a way that boundaries between different media coincide with element boundaries.

Different methods are available to discretize the second-order time derivative in Eq. (1), both explicit and implicit, e.g. the leapfrog-method (Bathe, 1996), the Wilson cycle (Zienkiewicz and Taylor, 2000) or the Newmark-algorithm (Newmark, 1959; Hughes, 1987). In this study a variation of the implicit Newmark-algorithm is applied (Zienkiewicz and Taylor, 2000). It uses a predictor–corrector scheme and calculates the displacement field **u** as the primary unknown, unlike the classical Newmark-algorithm that calculates the acceleration **a** as the first unknown.

- Predictor:

$$
\begin{aligned}
\mathbf{a}_{i+1}^{\text{prediction}} &= -\frac{1}{\beta\,\Delta t^2}\mathbf{u}_i - \frac{1}{\beta\,\Delta t}\mathbf{v}_i - \frac{1-2\beta}{2\beta}\mathbf{a}_i \\
\mathbf{v}_{i+1}^{\text{prediction}} &= -\frac{\gamma}{\beta\,\Delta t}\mathbf{u}_i + \left(1-\frac{\gamma}{\beta}\right)\mathbf{v}_i + \left(1-\frac{\gamma}{2\beta}\right)\Delta t\mathbf{a}_i
\end{aligned}
\tag{2}
$$

- Solution:

$$
\mathbf{u}_{i+1} = -\left(\frac{1}{\beta\,\Delta t^2}\mathbf{M}+\mathbf{K}\right)^{-1}(\mathbf{M}\mathbf{a}_{i+1}^{\text{prediction}})
\tag{3}
$$

- Corrector:

$$
\begin{aligned}
\mathbf{a}_{i+1} &= \mathbf{a}_{i+1}^{\text{prediction}} + \frac{1}{\beta\,\Delta t^2}\mathbf{u}_{i+1} \\
\mathbf{v}_{i+1} &= \mathbf{v}_{i+1}^{\text{prediction}} + \frac{\gamma}{\beta\,\Delta t}\mathbf{u}_{i+1}
\end{aligned}
\tag{4}
$$

In Eqs. (2)–(4) i is the index of any discrete time interval, Δt is the time increment, **u**, **v** and **a** are the two-dimensional displacement, velocity and acceleration fields, respectively, **M** is the lumped mass matrix and **K** is the stiffness matrix. For β and γ

the optimal values of 1/4 and 1/2 are chosen (Newmark, 1959; Bathe, 1996). For explicit time integration the classical Newmark-algorithm (Newmark, 1959; Hughes, 1987) is used. It is also a predictor–corrector method but calculates the acceleration field **a** as the first unknown. To make this algorithm explicit β is set to zero.

3.3. FEM in both time and space

Applying the FEM in the temporal domain can be traced back to the seminal work of Argyris and Scharpf (1969) and of Fried (1969). Here, a time-discontinuous Galerkin method (DGT) is applied (Chen et al., 2006). The DGT method is based on classical C_0-continuous interpolation and test functions in the spatial domain, and discontinuous interpolation and test functions in the temporal domain, respectively (Fig. 5). The actual elements used were 6-node triangu-
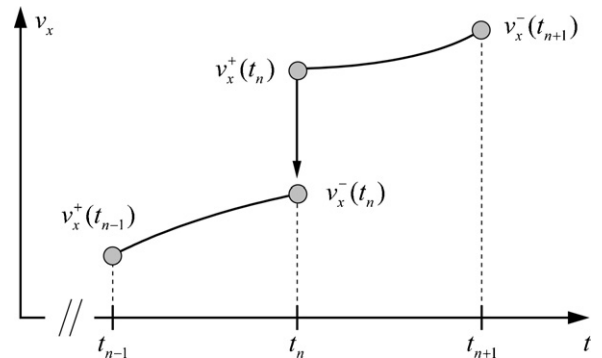

Fig. 5. Discontinuous interpolation functions of the time-discontinuous Galerkin method (DGT) in the time domain. At time t_n two degrees of freedom for v_x are necessary, one for the time-element $[t_{n-1}\ t_n]$ and one for the time-element $[t_n\ t_{n+1}]$.

lar elements with biquadratic continuous interpolation functions in space and linear discontinuous interpolation functions in time. FEM-meshes are created by a Delaunay-type mesh generator (GID-CIMNE). Furthermore, the hybrid velocity integration (HVI) method is applied, which is based on a pure velocity formulation of the governing first-order equations in time. According to the applied discontinuous interpolation functions in the temporal domain, the inherent displacement field can be calculated in a subsequent, i.e. post-processing step. Thus, a classical solution technique based on the numerical investigation of a set of first-order equations in time can be circumvented. Technical details and further numerical comparisons between classical FEM schemes and DGT or HVI techniques are explained by Chen et al. (2008). According to the classical Bubnov–Galerkin scheme, interpolation and test functions belong to the same function space leading to an algebraic system of equations with symmetric matrices. In the present numerical scheme, the temporal inter-element continuity is enforced by a special flux treatment technique (Chen et al., 2006). Thus, stable and efficient numerical results with a low amount of numerical dispersion and dissipation are obtained with rather large time steps.

3.4. Analytical solution

The analytical solution of the scattering problem displayed in Fig. 1a is described by Liu et al. (2000). It provides the full seismogram at any synthetic receiver in the model domain. Such a synthetic receiver is defined in terms of cylindrical coordinates r and θ for a coordinate system centred at the inclusion center. The solution in terms of displacement potentials takes the following form for synthetic receivers outside the inclusion:

$$\varphi(t, r, \theta) = \int_{-\infty}^{+\infty} G(\omega) \left(\sum_{m=0}^{+\infty} A_m H_m^{(1)}(k_P r) \cos(m\theta) \right) e^{-i\omega t} \, d\omega, \quad (5)$$

$$\psi(t, r, \theta) = \int_{-\infty}^{+\infty} G(\omega) \left(\sum_{m=1}^{+\infty} B_m H_m^{(1)}(k_S r) \sin(m\theta) \right) e^{-i\omega t} \, d\omega. \quad (6)$$

In Eqs. (5) and (6) φ and ψ are the displacement potentials of the P- and the S-wave, respectively, G is the complex-valued frequency spectrum of the displacement potential of the incident wave, ω is angular frequency, $H_m^{(1)}$ is the Hankel function of the first kind of order m and k_P and k_S are the wave numbers of the P- and the S-wave, respectively. The two rather complicated coefficients A_m and B_m are given in the Appendix of Liu et al. (2000) and are determined

from the boundary condition at the inclusion interface. To get the final solution the integrals from $-\infty$ to $+\infty$ and the summations over m have to be calculated numerically. Both the number of summands and the finite integration and summation boundaries are chosen in a way that the summation converges to a constant value. From Eqs. (5) and (6) the displacement field of the scattered wave can be separated into P- and S-wave fields ($\mathbf{u}^P$ and $\mathbf{u}^S$), each separated into x- and y-components (u_x^i and u_y^i) using

$$u_x^P(t, x, y) = \frac{\partial \varphi(t, r, \theta)}{\partial r} \cos \theta - \frac{1}{r} \frac{\partial \varphi(t, r, \theta)}{\partial \theta} \sin \theta, \quad (7)$$

$$u_y^P(t, x, y) = \frac{\partial \varphi(t, r, \theta)}{\partial r} \sin \theta + \frac{1}{r} \frac{\partial \varphi(t, r, \theta)}{\partial \theta} \cos \theta, \quad (8)$$

$$u_x^S(t, x, y) = \frac{1}{r} \frac{\partial \psi(t, r, \theta)}{\partial \theta} \sin \theta - \frac{\partial \psi(t, r, \theta)}{\partial r} \cos \theta, \quad (9)$$

$$u_y^S(t, x, y) = \frac{1}{r} \frac{\partial \psi(t, r, \theta)}{\partial \theta} \cos \theta + \frac{\partial \psi(t, r, \theta)}{\partial r} \sin \theta. \quad (10)$$

4. Results

In Fig. 6 the synthetic seismograms at the receiver location indicated in Fig. 1a are plotted as gray lines for all different numerical methods and for different spatial and temporal resolutions. In Table 2 numerical parameters of all performed simulations are given. The black lines in Fig. 6 are calculated using the analytical solution of Liu et al. (2000). In y-direction (Fig. 6a) the first event recorded is the incident plane P-wave. Later events are the scattered P-wave and the scattered S-wave (P-to-S-converted) that are overlapping and, therefore, not distinguishable. In x-direction (Fig. 6b) the incident wave is not present and only the scattered wave field is recorded. The lowest-resolution numerical simulations differ significantly from the analytical solution, especially towards the end of the seismogram. However, the majority of the simulations fit the analytical solution very well. This applies for the shape of the seismogram, amplitudes and arrival times. The seismograms in Fig. 6 are used to calculate the L2 error norm in both x- and y-directions,

$$\text{L2}_{x,y} = \sqrt{\frac{\sum_{i=1}^{nt} (u_{x,y}^{\text{num}}(t_i) - u_{x,y}^{\text{ana}}(t_i))^2}{\sum_{i=1}^{nt} (u_{x,y}^{\text{ana}}(t_i))^2}}, \quad (11)$$

where u_i^{num} is the particle displacement obtained from a numerical simulation and u_i^{ana} is the particle displacement obtained analytically. Fig. 7 compares the L2 error norm for displacements in x- and y-direction for the different numerical methods. The errors in the
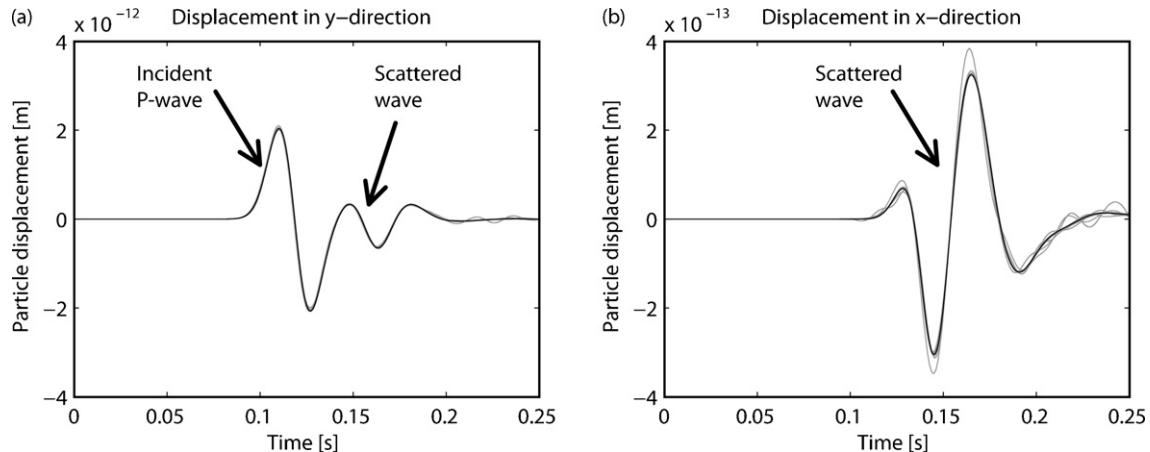

Fig. 6. Synthetic seismograms (displacement–time–signal) at the receiver shown in Fig. 1a. Gray lines show seismograms obtained from numerical simulations for all different numerical methods. Black lines are the synthetic seismograms obtained analytically. (a) Particle displacement in y-direction and (b) x-direction. Note the different scales in the two subfigures.

Table 2
Numerical parameters for all simulations performed in this study

	Method in space							
	FDM	FEM			FEM	FEM		
	expl. FDM[a]	impl. FDM[a]			expl. FDM[a]	impl. FEM[a]		
# Nodes	1,490,841	216,705			216,705	287,725		
# Nodes inside inclusion	20,108	21,392			21,392	4144		
Δt ($\times 10^{-5}$ s)	7.04	23.7	11.9	2.96	0.64	23.7	11.9	2.96
# Nodes	1,002,001	112,409			112,409	128,369		
# Nodes inside inclusion	15,380	5516			5516	3528		
Δt ($\times 10^{-5}$ s)	8.05	23.7	11.9	2.96	1.43	23.7	11.9	2.96
# Nodes	549,081	40,049			40,049	72,821		
# Nodes inside inclusion	7860	826			826	3528		
Δt ($\times 10^{-5}$ s)	11.3	23.7	11.9	2.96	5.38	23.7	11.9	2.96
# Nodes	212,521	10,349			10,349	33,405		
# Nodes inside inclusion	1976	210			210	3528		
Δt ($\times 10^{-5}$ s)	22.5	23.7	11.9	2.96	13.8	23.7	11.9	2.96
# Nodes	40,401					13,249		
# Nodes inside inclusion	80					3528		
Δt ($\times 10^{-5}$ s)	110					23.7	11.9	2.96
# Nodes						9089		
# Nodes inside inclusion						3528		
Δt ($\times 10^{-5}$ s)						23.7	11.9	2.96
# Nodes						7005		
# Nodes inside inclusion						3528		
Δt ($\times 10^{-5}$ s)						23.7	11.9	2.96

Nodes is the total number of numerical nodes in the domain, # Nodes inside inclusion is the number of numerical nodes that belong to the inclusion, Δt is the time increment in 10^{-5} s, expl. refers to explicit time integration and impl. refers to implicit time integration. Explicit time increments are calculated using the von Neumann stability criterion. The three different implicit time increments are chosen freely.

[a] Method in time.

two directions follow approximately a linear trend with increasing resolution whereas the error for displacement in y-direction is consistently smaller than in x-direction. This is already visible in Fig. 6. For further analysis only the y-component of the displacement (Fig. 6a) is considered. Due to the linear trend of the errors in the two directions (Fig. 7), results of the error analysis for displacements in x-direction are comparable.

In the following sections the accuracy of the different numerical methods is analyzed as a function of spatial and temporal resolu-

Fig. 7. L2 error norm for particle displacement in y-direction plotted versus L2 error norm for particle displacement in x-direction. Different lines correspond to different numerical methods and/or different implicit time increments. First abbreviations in the legend before the comma (FDM or FEM) stands for the spatial discretization method, second abbreviation stands for the time discretization whereas expl. refers to explicit time integration and impl. refers to implicit time integration. Implicit time increments for both temporal FDM and temporal FEM are: 1, $\Delta t = 2.37 \times 10^{-4}$ s; 2, $\Delta t = 1.19 \times 10^{-4}$ s; 3, $\Delta t = 2.96 \times 10^{-5}$ s.

tion (Table 2). For explicit methods spatial and temporal resolutions are not independent from each other because the time increment is calculated with the von Neumann stability criterion, which is a function of the spatial resolution. Therefore, effects of spatial and temporal resolutions cannot be separated completely for explicit methods.

4.1. Effect of spatial resolution

With each numerical method a series of simulations with changing spatial resolution was performed (Table 2). Fig. 8 shows the L2 error norm for the particle displacement in y-direction as a function of the number of degrees of freedom for the different methods. Fig. 8a considers the total number of degrees of freedom in the whole numerical domain and Fig. 8b considers only the degrees of freedom inside the inclusion. All methods become more accurate with increasing spatial resolution. However, for the same number of degrees of freedom (Fig. 8a) the spatial FEM is more than one order of magnitude more accurate than the spatial FDM. Also, the method using the FEM in space and the implicit FDM in time clearly shows an effect of the chosen time increment. Larger time increments give less accurate results and the difference in accuracy increases with increasing spatial resolution. At the same time the method using the FEM in both space and time does not show this effect and the lines for the two different time increments lie virtually on top of each other.

The results change considerably when only the number of degrees of freedom inside the heterogeneity (Fig. 8b) is considered. Methods using the FEM in space are still more accurate than the FDM in space but the difference is much smaller. This is largely due to the fact that the numerical FEM-mesh can vary significantly while the spatial variation of the FDM-mesh is limited. The method using the FEM in space and the FDM in time makes use of this advan-
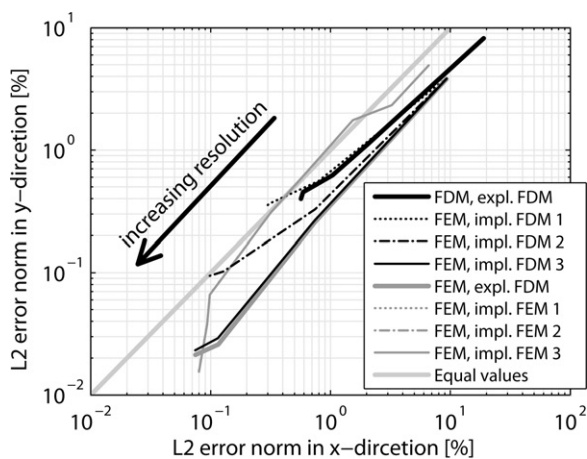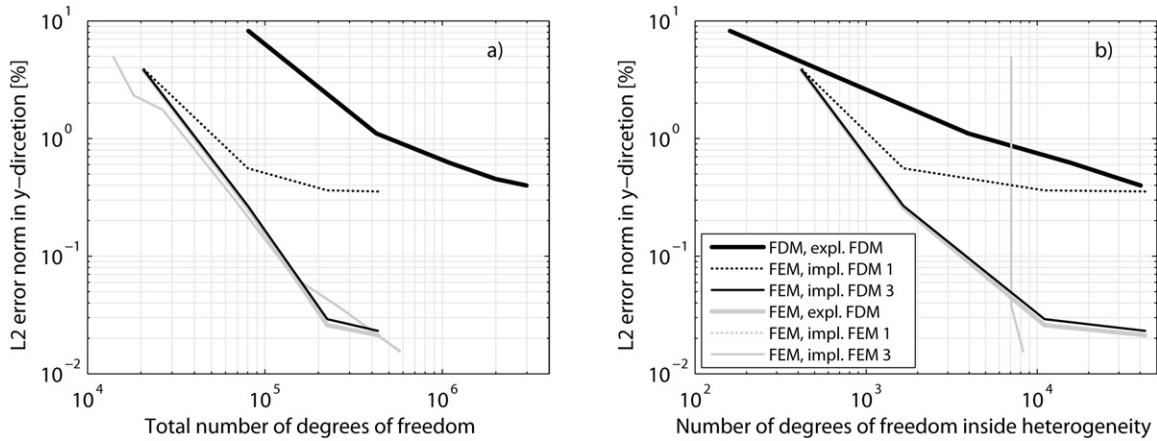
Fig. 8. L2 error norm for particle displacement in *y*-direction plotted versus (a) total number of degrees of freedom in the numerical domain and (b) number of degrees of freedom inside the circular inclusion. The legend is valid for both subfigures and is explained in detail in Fig. 7.

tage. The spatial resolution is increased inside and at the boundary of the inclusion while the resolution outside the inclusion is considerably lower. The meshgenerator used by the method using the FEM in space and the FEM in time keeps the resolution inside and at the boundary of the inclusion constant while the resolution in the surrounding media is increased (Table 2). This leads to the almost vertical line in Fig. 8b.

Fig. 9 is similar to Fig. 8 but uses as a measure for spatial resolution the number of numerical nodes per dominant wavelength (157.1 m). Because the spatial resolution can vary within the numerical domain (for both the spatial FEM and the spatial FDM) two measures are considered. Fig. 9a considers the minimal and Fig. 9b considers the maximal distance between two neighboring nodal points within the whole numerical domain. The minimal distance between two nodal points (i.e. highest spatial resolution) is on the boundary of the inclusion for all methods. Therefore, Figs. 8b and 9a look very similar. However, the line representing the spatial FDM is shifted even more to the left relative to the lines representing spatial FEM compared to Fig. 8a and b. Again, this is an effect of the varying grid spacing of the spatial FEM-mesh. Also the discrepancy between Fig. 9a and b can be explained with the unstructured FEM-mesh. While the grid spacing for the spatial FDM does not vary significantly, the FEM-mesh can have larger spacing away from the inclusion. This shifts all lines representing the spatial FEM to the left relative to the spatial FDM in Fig. 9b compared to Fig. 9a.
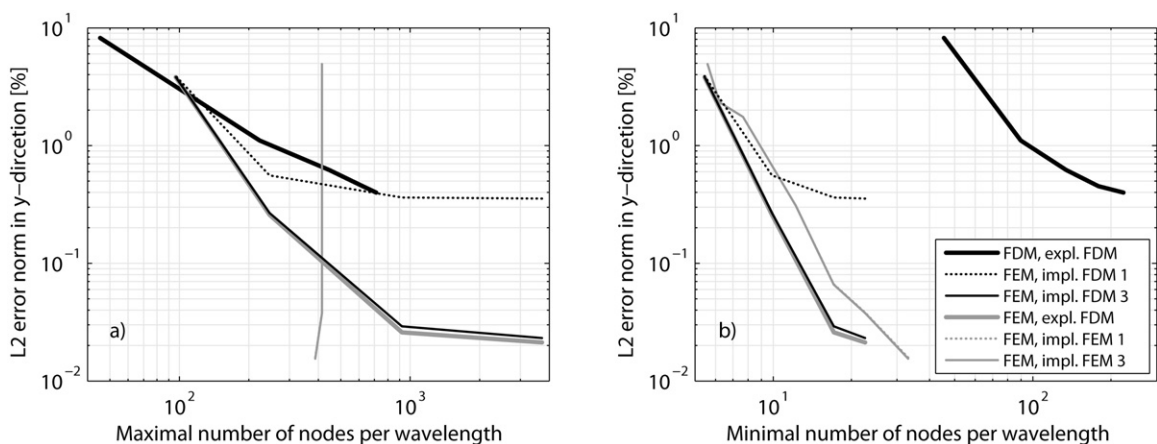
4.2. Effect of temporal resolution

While for explicit schemes the time increment decreases with increasing spatial resolution according to the von Neumann stability criterion, no such criterion exists for implicit schemes and the time increment can be chosen freely. To test the effect of temporal resolution implicit simulations were performed with three different time increments (Table 2). Fig. 10 shows the L2 error norm for the particle displacement in *y*-direction as a function of the time increment used in the simulations. Considering only the two explicit schemes, Fig. 10 resembles Fig. 9a. The difference is a result of the two slightly different stability criteria for the explicit time increments that were applied to the spatial FDM and spatial FEM. The spatial FEM results in a smaller explicit time increment because the numerical mesh can be locally very fine whereas the FDM-mesh is more uniform. However, the two explicit schemes follow a common trend of increasing accuracy with decreasing time increment.

For implicit schemes the different lines in Fig. 10 represent simulations with the same spatial resolution but different time increments. For low spatial resolution there is no effect of the time increment. This means that the accuracy is limited by the spatial resolution. Thus, the time increment of the coupled space-time FEM could be even enlarged. However, for comparison reasons, this was not done in the present investigation, but was studied in detail in
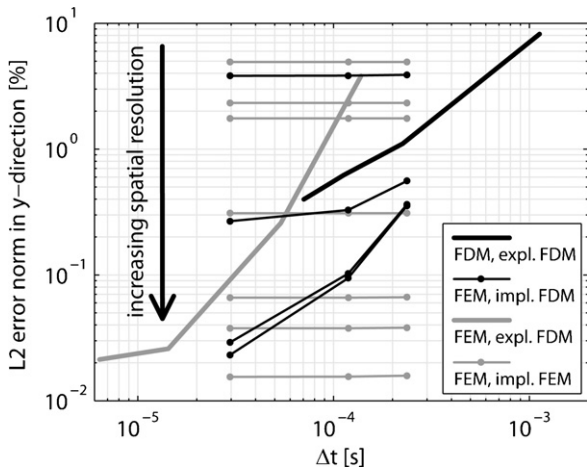

Fig. 9. L2 error norm for particle displacement in *y*-direction plotted versus number of numerical nodes per dominant wavelength. To calculate the number of nodes per dominant wavelength the shortest distance between two nodes in the whole numerical domain is used in (a). In (b) the longest distance between two nodes in the whole numerical domain is used. The legend is valid for both subfigures and is explained in detail in Fig. 7.

Fig. 10. L2 error norm for particle displacement in *y*-direction plotted versus the applied time increment. Abbreviations in the legend are explained in detail in Fig. 7. For implicit schemes the different lines represent the same spatial resolution but different time increments.

Chen et al. (2008). For higher spatial resolution the method using the FEM in space and the FDM in time clearly shows higher accuracy for smaller time increments. The accuracy for a given spatial resolution is limited by the applied time increments. The same accuracy can be achieved by using either a smaller time increment or a higher spatial resolution. At the same time the method using the FEM in both space and time is unaffected by the changing time increment for all spatial resolutions. The accuracy is limited by the spatial resolution.

4.3. Effect of computation time

The two numerical algorithms using the FDM in time are implemented in MATLAB while the algorithm using the FEM in time is implemented in C. Also, the different simulations were not all performed on the same computer. Therefore, it is difficult to compare all the simulations. However, Fig. 11 shows the L2 error norm for the particle displacement in *y*-direction as a function of computation time per time increment (Fig. 11a) and as a function of total computation time (Fig. 11b) for all performed simulations. For increasing resolution (i.e. higher accuracy) implicit calculations in C perform faster than in MATLAB.

To achieve a given accuracy the method using the FEM in space and the explicit FDM in time performs fastest. This is especially true when only one time increment is considered (Fig. 11a). Then the method using the FEM in space and the explicit FDM in time performs more than an order of magnitude faster than all other methods for a given accuracy. The unstructured FEM-mesh allows having a high spatial resolution at the inclusion boundary without the need of a high resolution away from the inclusion. This leads to accurate solutions with a much smaller number of total grid points compared to the spatial FDM and therefore also to faster performance. However, high resolution at the inclusion boundary also results in a small explicit time increment (von Neumann stability criterion) and therefore to a high number of time steps. Considering total computation time (Fig. 11b) the difference between the method using the FEM in space and the explicit FDM in time and all other methods is therefore smaller. However, it still performs a factor two (or more) faster than the other methods for a given accuracy.

Considering only one time increment (Fig. 11a) the implicit methods using the FEM in space perform as fast as the method using the FDM in both space and time, although this is an explicit method. The slower performance that is expected with implicit methods is compensated by the fact that the unstructured FEM-mesh needs much less numerical nodes for the same accuracy compared to spatial FDM (Fig. 8a). Due to the different numbers of time steps for the different methods the lines representing the different methods in Fig. 11b are much further apart from each other compared to Fig. 11a.

5. Discussion

The spatial FEM generally gives better results compared to the spatial FDM for the presented geometrical setup. The unstructured FEM-mesh allows a very accurate spatial approximation of the circular inclusion, or any other heterogeneity, without introducing a staircase-like material boundary. In addition, the unstructured FEM-mesh allows higher spatial resolution where it is needed without the need of high spatial resolution in other regions of the domain. This reduces the required number of grid points compared to the rectangular FDM-meshes. A desired accuracy can also be achieved with the spatial FDM, but a much higher number of numerical grid points is needed. This advantage of the spatial FEM will be even more important in three-dimensional simulations where the number of grid points increases more rapidly. Other methods, such as the finite volume method, are also able
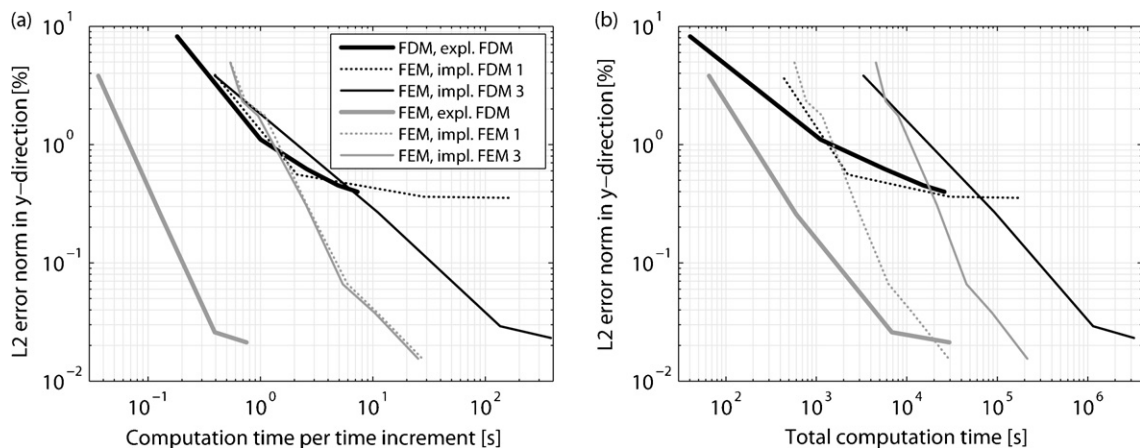

Fig. 11. L2 error norm for particle displacement in *y*-direction plotted versus (a) computation time (CPU time) per time increment and (b) total computation time (CPU time) for the whole simulation. The legend is valid for both subfigures and is explained in detail in Fig. 7.

to handle unstructured meshes and are expected to show similar accuracies as the spatial FEM. Taking the aspect of computation time into account, the best method shown in this study is the FEM in space and the explicit FDM in time. It has both the advantage of the unstructured mesh and of the fast explicit time integration. Simulations are both accurate and fast.

From a programming point of view the spatial FDM is the simplest numerical method and is also commonly used for numerical wave propagation simulations. Therefore, it is worth to evaluate the desired accuracy and calculation time for a particular problem. For many applications the spatial FDM gives accurate enough results and/or the resolution can be set high enough to provide the desired accuracy. A further advantage is that no third-party mesh generator is necessary for the spatial FDM. Therefore, the numerical mesh is under full control. The spatial FEM with the FDM in time is slightly more complex to implement but leads to more accurate results. The space–time FEM algorithm is more complex and is not a trivial extension of the spatial FEM with the FDM in time. For discontinuous elements in time used here each spatial nodal point requires twice as many degrees of freedom compared to the spatial FEM with the FDM in time. Interpolation functions in time have to be independent of interpolation functions in space and integration schemes have to be varied. The space–time FEM is compared quantitatively and qualitatively with the spatial FEM combined with the FDM in time by Chen et al. (2006, 2008). A big advantage is the fact that it is straight forward to implement interpolation functions that are higher order in time (e.g. second or fourth order) that result in a higher convergence rate. In the ideal case interpolation functions in time adapt to the actual problem solved.

The analytical solution provided by Liu et al. (2000) is expressed as integrals and sums (Eqs. (5) and (6)) that need to be calculated numerically. This results in a relatively lengthy numerical algorithm. It has to be made sure that the number of summands and the finite boundaries for integration and summation are chosen in a way that the solution converges. The seismogram (displacement–time–signal) for a synthetic receiver can be calculated with reasonable computation time because the number of time increments used is not too big. A snapshot as in Fig. 1 for a high spatial resolution would need a large computational effort. Also, the coefficients of the analytical solution are so complicated and long that it is difficult to gain good physical insight in the scattering process from the provided formulas.

Generally, the comparison between the different methods is not straight forward. In explicit schemes spatial resolution and the time increment are tightly coupled through the von Neumann stability criterion. Therefore, the effect of the two on the accuracy of the numerical solution cannot easily be separated. The spatial FDM and the spatial FEM use a completely different numerical mesh. Therefore, it is also difficult to compare the spatial resolution of the two methods and several attributes describing the spatial resolution have to be considered for comparison.

6. Conclusions

The analytical solution for the simple scattering problem studied here is in fact expressed as infinite integrals and sums. It is therefore not a pure analytical solution and a numerical algorithm is required to calculate the values of the analytical solution. For more geometrically complicated scattering problems numerical methods become essential.

The FDM and the FEM are two different numerical methods to spatially discretize the geometry of the scattering problem. Both methods have advantages and disadvantages but the main advantage of the FEM is the application of unstructured numerical meshes while the FDM needs rectangular meshes. Therefore, the FEM provides the same numerical accuracy as the FDM but requires significantly less numerical grid points. This is a result of the unstructured mesh that allows high resolution where it is needed with lower resolution elsewhere in the model domain. Also, the boundaries of heterogeneities can be better resolved with unstructured meshes and the FEM does not require interpolation of material properties which is required for the FDM using a velocity–stress formulation on a staggered grid. On the other hand, an advantage of the FDM is the considerably simpler numerical implementation.

The results show that the numerical accuracy does not improve by using implicit time integration schemes (FDM or FEM) instead of explicit ones (FDM). Therefore, for the presented geometrical setup of a circular inclusion inside a homogeneous medium, the numerical algorithm consisting of the FEM in space combined with the explicit FDM in time is the best choice which provides accurate results and performs fastest.

References

Achenbach, J.D., 1973. Wave Propagation in Elastic Solids. North-Holland Series in Applied Mathematics and Mechanics. North-Holland Publishing Company, Amsterdam, ISBN: 0-7204-2367-8.

Aki, K., Richards, P.G., 1980. Quantitative Seismology: Theory and Methods. W.H. Freeman and Company, San Francisco, ISBN: 0-7167-1058-7.

Ames, W.F., 1992. Numerical Methods for Partial Differential Equations. Academic Press Inc., San Diego, ISBN: 0-12-056761-X.

Argyris, J.H., Scharpf, D.W., 1969. Finite Elements in Time and Space. Nuclear Engineering and Design 10 (4), 456–464.

Bathe, K.-J., 1996. Finite Element Procedures. Prentice Hall, Upper Saddle River, NJ, ISBN: 0-13-301458-4.

Ben-Menahem, A., Jit Singh, S., 1981. Seismic Waves and Sources. Springer Verlag, New York, ISBN: 0-387-90506-5.

Bohlen, T., Saenger, E.H., 2006. Accuracy of heterogeneous staggered-grid finite-difference modeling of Rayleigh waves. Geophysics 71 (4), T109–T115.

Carcione, J.M., Cavallini, F., Santos, J.E., Ravazzoli, C.L., Gauzellino, P.M., 2004. Wave propagation in partially saturated porous media: simulation of a second slow wave. Wave Motion 39 (3), 227–240.

Carcione, J.M., Helle, H.B., Pham, N.H., 2003. White's model for wave propagation in partially saturated rocks: comparison with poroelastic numerical experiments. Geophysics 68 (4), 1389–1398.

Carcione, J.M., Herman, G.C., ten Kroode, A.P.E., 2002. Seismic modeling. Geophysics 67 (4), 1304–1325.

Cerveny, V., 2001. Seismic Ray Theory. Cambridge University Press, Cambridge, ISBN: 0-521-36671-2.

Chen, Z.Y., Steeb, H., Diebels, S., 2006. A time-discontinuous Galerkin method for the dynamical analysis of porous media. International Journal for Numerical and Analytical Methods in Geomechanics 30 (11), 1113–1134.

Chen, Z.Y., Steeb, H., Diebels, S., 2008. A new hybrid velocity integration method applied to elastic wave propagation. International Journal for Numerical Methods in Engineering 74 (1), 56–79.

Cohen, G.C., 2002. Higher-order Numerical Methods for Transient Wave Equations. Springer Verlag, Berlin, ISBN: 3-540-41598-X.

Fried, I., 1969. Finite-element analysis of time-dependent phenomena. AIAA Journal 7 (6), 1170–1173.

Higham, N.J., 1996. Accuracy and Stability of Numerical Algorithms. Society for Industrial & Applied Mathematics, Philadelphia, ISBN: 0-89871-355-2.

Hughes, T., 1987. The Finite Element Method: Linear Static and Dynamic Finite Element Analysis. Dover Publications, Mineola, NY, ISBN: 0-486-41181-8.

Kelly, K.R., Marfurt, K.J., 1990. Numerical Modeling of Seismic Wave Propagation. Geophysics Reprint Series, 13. Society of Exploration Geophysicists, Tulsa, OK, ISBN: 1-56080-011-9.

Korneev, V.A., Johnson, L.R., 1996. Scattering of P and S waves by a spherically symmetric inclusion. Pure and Applied Geophysics 147 (4), 675–718.

Kruger, O.S., Saenger, E.H., Shapiro, S.A., 2005. Scattering and diffraction by a single crack: an accuracy analysis of the rotated staggered grid. Geophysical Journal International 162 (1), 25–31.

Lindsay, R.B., 1960. Mechanical Radiation. International Series in Pure and Applied Physics. McGraw-Hill, New York, ISBN: 00-703784-40.

Liu, Y.B., Wu, R.S., Ying, C.F., 2000. Scattering of elastic waves by an elastic or viscoelastic cylinder. Geophysical Journal International 142 (2), 439–460.

Love, A.E.H., 1927. A Treatise on the Mathematical Theory of Elasticity. Dover Publications, New York, ISBN: 0-486-60174-9.

Masson, Y.J., Pride, S.R., 2007. Poroelastic finite difference modeling of seismic attenuation and dispersion due to mesoscopic-scale heterogeneity. Journal of Geophysical Research-Solid Earth 112 (B3).

Mavko, G., Mukerji, T., Dvorkin, J., 1998. The Rock Physics Handbook. Cambridge University Press, Cambridge, ISBN: 0-521-54344-4.

Moczo, P., Kristek, J., Vavrycuk, V., Archuleta, R.J., Halada, L., 2002. 3D heterogeneous staggered-grid finite-difference modeling of seismic motion with volume harmonic and arithmetic averaging of elastic moduli and densities. Bulletin of the Seismological Society of America 92 (8), 3042–3066.

Moczo, P., Robertsson, J.O.A., Eisner, L., 2007. The finite-difference time–domain method for modeling seismic wave propagation. Advances in Geophysics 48, 421–516, ISSN: 0065-2687.

Moser, T.J., Pajchel, J., 1997. Recursive seismic ray modelling: applications in inversion and VSP. Geophysical Prospecting 45 (6), 885–908.

Newmark, N.M., 1959. A method of computation for structural dynamics. Journal of the Engineering Mechanics Division, Proceedings of the American Society of Civil Engineers, 67–94.

Saenger, E.H., Ciz, R., Krüger, O.S., Schmalholz, S.M., Gurevich, B., Shapiro, S.A., 2007. Finite-difference modeling of wave propagation on microscale: a snapshot of the work in progress. Geophysics 72, SM293–SM300.

Saenger, E.H., Gold, N., Shapiro, S.A., 2000. Modeling the propagation of elastic waves using a modified finite-difference grid. Wave Motion 31 (1), 77–92.

Sanchez-Sesma, F.J., Iturraran-Viveros, U., 2001. Scattering and diffraction of SH waves by a finite crack: an analytical solution. Geophysical Journal International 145 (3), 749–758.

Santos, J.E., Ravazzoli, C.L., Gauzellino, P.M., Carcione, J.M., 2005. Numerical simulation of ultrasonic waves in reservoir rocks with patchy saturation and fractal petrophysical properties. Computational Geosciences 9 (1), 1–27.

Shewchuk, J.R., 1996. Triangle: engineering a 2D quality mesh generator and Delaunay triangulator. In: Ming, C.L., Dinesh, M. (Eds.), Applied Computational Geometry: Towards Geometric Engineering. Lecture Notes in Computer Science. Springer Verlag, Berlin, pp. 203–222, ISBN: 3-540-61785-X.

Shewchuk, J.R., 2002. Delaunay refinement algorithms for triangular mesh generation. Computational Geometry 22 (1–3), 21–74.

Smith, G.D., 1985. Numerical Solutions of Partial Differential Equations: Finite Difference Methods. Oxford University Press, New York, ISBN: 0-19-859650-2.

Virieux, J., 1986. P-Sv-wave propagation in heterogeneous media—velocity–stress finite-difference method. Geophysics 51 (4), 889–901.

White, R.M., 1958. Elastic wave scattering at a cylindrical discontinuity in a solid. Journal of the Acoustical Society of America 30 (8), 771–785.

Ying, C.F., Truell, R., 1956. Scattering of a plane longitudinal wave by a spherical obstacle in an isotropically elastic solid. Journal of Applied Physics 27 (9), 1086–1097.

Zienkiewicz, O.C., Taylor, R.L., 2000. The Finite Element Method, vol. 1: The Basis. Butterworth-Heinemann, Oxford, ISBN: 0-7506-5049-4.